ARTICLE OPEN

Check for updates

Flexible organic integrated electronics for self-powered multiplexed ocular monitoring

Baojun Lin[1,4], Meng Wang[1,4], Chao Zhao[1], Shijie Wang[1], Kai Chen[1], Xiao Li[1], Zaishang Long[1], Chenxu Zhao[2], Xinyue Song[3], Sen Yan[3], Laili Wang[2]✉ and Wei Ma[1]✉

Smart contact lens has drawn extensive research interests due to the noninvasive real-time detection of the human body to provide biomedical information for health management. However, it has been difficult to accurately measure the physiological signals in tears, and the use of external power source has also hindered the future applications. Here, we demonstrated an organic electrochemical transistor based multiplexed sensors self-powered by the organic solar cells (OSCs). The integrated device was fabricated via simple process including solution blade-coating and thermal evaporation. OSCs were optimized to provide optimal operation voltage for the sensors that exhibit semilog-linear response to the glucose and calcium ions in tear fluids without any peripheral circuits. The sensing signals can be transmitted to the laptop wirelessly through a near filed communication unit. This integrated self-powered multiplexed sensing device will provide real-time monitoring of the biomarkers in tears, prospected to be installed on the smart contact lens for the early detection and diagnosis of diabetes.

npj Flexible Electronics (2022)6:77 ; https://doi.org/10.1038/s41528-022-00211-6

INTRODUCTION

Bioelectronic devices capable of real-time monitoring health status and biomedical information of human body have been widely investigated over the past decades as a key of next-generation wearable electronics[1–8]. Numerous wearable devices have been developed successfully in electrocardiography[9], photoplethysmography, pulse oximetry[10] and glucose monitoring[11–13], yet still limited by the rigid circuit, terminal connection and power supply. Organic semiconducting devices, such as organic electrochemical transistors (OECTs), organic photodetectors (OPDs) and organic light emitting diodes (OLEDs), have shown great potential in wearable devices due to their inherent light-weight, flexibility, and biological compatibility[14–16]. Great progress has been made in in-vitro wearable devices by integrating the OECTs and OPDs with biofuel cells[17–20], lithium batteries[21,22], and wireless communication units[14,23–25] to achieve the monitoring of signals from sweat and other physiological signals in the past years.

Among various wearable bioelectronics, smart contact lenses have attracted commercial attention for in-vivo health monitoring[14,23,24,26–30]. Tears could serve as a convenient and noninvasive object to monitor the physiological conditions in human body which can be collected in the contact lens naturally and used to assess various biomarkers such as glucose, sodium ions, potassium ions[31–33]. Thus, a contact lens equipped with sensors provide a noninvasive sensing method to monitor metabolites from in tears. For numerous biomarkers, glucose is a characteristic signal for the diagnosis and management of diabetes. Presently, for diabetes patients, the finger prick method has to be used every day to monitor the glucose level in blood. To achieve convenient and painless detection, Google collaborated with Novartis proposed the Google Lens for the diagnosis of diabetic patients in 2014. However, this program has been terminated 2 years later since the lens cannot establish the response to the blood glucose level accurately. In addition to the concentration change of glucose, many concurrent physiological components change in the body fluids of patients. For example, calcium ions (Ca^{2+}) have been reported to be related with the release of the insulin[34,35]. The elevated Ca^{2+} levels are associated with impaired glucose metabolism, which means a higher risk of diabetes. Under this consideration, developing multiplexed sensing of diverse biomarker in tears could provide more precise early warning and diagnosis of diseases. However, up to now, most of the commercial ion detection instruments are based on the chromatographic method that requires large volumes of liquids (about 10 mL). Compared to the chromatographic methods, OECT sensors combining ions selective membrane have been reported widely[36–38] and succeeded in ion detection in small amount of sweats, which provides the equipment foundation for ion detection in tears.

Power supply is one other key limiting factors of wearable bioelectronics. Batteries have been used as the primary power source for current vitro wearing devices which suffer from the risk of insufficient long-term availability and uncomfortableness for in vivo electronics. For next-generation bioelectronics, the self-powering functionality should be equipped while the bulky external power supplies and wirings should be avoided. So far, numerous instances on the nanogenerators and biofuel cells have been reported for wearable and implantable bioelectronic devices[17,18,39,40]. However, due to the low energy conversion efficiency and unstable energy sources, these power supplies are hard to satisfy the energy demand of complex sensing and signal transmission system. By contrast, solar cells provide a higher power output even under the indoor illumination conditions. Among all the photovoltaic cells, organic solar cells (OSCs) have exhibited advantages in output management and flexible devices since the output voltage and current can be modulated readily by photovoltaic materials modification and matching. Thus, the

[1]State Key Laboratory for Mechanical Behavior of Materials, Xi'an Jiaotong University, Xi'an, China. [2]State Key Laboratory of Electrical Insulation and Power Equipment, Xi'an Jiaotong University, Xi'an, China. [3]School of Information and Communications Engineering, Xi'an Jiaotong University, Xi'an, China. [4]These authors contributed equally: Baojun Lin, Meng Wang. ✉email: LLwang@mail.xjtu.edu.cn; msewma@xjtu.edu.cn

output of power sources can be controlled according to the requirement of flexible biosensors to realize the high capability of sensing and monitoring without the usage of resistance and other circuit elements. However, to achieve controllable power supply of OSCs to the sensors, complicated processes such as photoetching are needed. A scalable method for the easy realization of integrated power sources should be developed.

To address these problems, here, we report a flexible and self-powered integrated OECT sensor for multiplexed sensing of glucose and Ca^{2+} in tears. Poly(2,3-dihydrothieno-1,4-dioxin)-poly (styrenesulfonate) (PEDOT:PSS) based OECT sensors with high transconductance were optimized to enhance the response to the biomarkers in tears. The output of OSCs were adjusted by the photovoltaic material matching to meet the demands of glucose and Ca^{2+} sensors. The gate and drain electrodes of both sensors are powered separately by four OSCs processed by patterned sequential blade-coating methods. The integrated system works well under normal LEDs illumination and displays nearly semilog-linear response to the concentration of glucose and Ca^{2+}. Furthermore, by connecting with a commercial RFID board, the information about the marker concentration can be transmitted to the portable devices like laptops wirelessly. Finally, the integrated multiplexed devices were implemented successfully to monitor the level changes of glucose and Ca^{2+} in tears, collected at different time points in a day. This integrated device is expected to be installed on the contact lens to achieve self-powered in-vivo wearable devices.

RESULTS AND DISCUSSION

Electrical characterization and morphology optimization of PEDOT:PSS based OECT sensors

Figure 1a illustrates the layout of the integrated system of the OSCs-powered multiplexed sensing devices for glucose and Ca^{2+} monitoring. This system consists of two parts, (i) two groups of OSCs including one inverted cell working as the power supply for the gate electrode and one conventional cell powering for the drain electrode while the bottom electrodes of OSCs are connected to the source electrodes of sensors, and (ii) two separated PEDOT:PSS based OECT (p-OECT) sensors. For Ca^{2+} selective monitoring, the Ca^{2+} selective membrane is coated on the PEDOT:PSS channel (Ca^{2+} OECT, c-OECT); for glucose sensing, the platinum gate is modified by the mixture of chitosan and glucose oxidase (glucose OECT, g-OECT). Enzymes immobilized on the gate electrode catalyze the glucose to produce peroxide (H_2O_2) and the electrochemical oxidation of H_2O_2 is catalyzed by the platinum electrode when a positive bias is applied. The oxidation process results in the transfer of electrons to the gate electrode and changes the electrical double layer at the gate/electrolyte interface, which reduces the voltage drop at the gate/electrolyte interface and hence increases the potential that is applied to the active channel and decrease the drain current. Supplementary Fig. 1 provides the detailed structure parameters of the integrated device and Supplementary Fig. 2 provides the fabrication process of different functional layers.

We first optimized the PEDOT:PSS channel layer to obtain high transconductance (g_m), a key parameter helps to capture the small concertation change in biomarkers. The ethylene glycol (EG) treatment[41] is a commonly used method for fabricating p-OECTs as it promotes the phase segregation of surplus PSS and improve the film crystallization. As shown in Fig. 1b, with the content of EG increasing to 5% volume fraction, g_m enhances about twice compared to the device without EG treatment. However, further increasing EG content decreases g_m. Thermal annealing is another commonly used method to enhance the polymer crystallization[42]. As shown in Fig. 1c, g_m increases to about 10 mS with 90 °C annealing treatment first and get decreased as the annealing temperature increases further. The transconductance difference of the p-OECTs with various treatments are further investigated by the grazing wide angle X-ray scattering (GIWAXS) measurement[43]. As shown in Fig. 1d and Supplementary Fig. 3, the PEDOT:PSS films show peaks at $\mathbf{q} = 1.38\ Å^{-1}$ (known as PSS halo) and ~$1.78\ Å^{-1}$ in the out-of-plane direction (π-π stacking in PEDOT)[41]. The coherence lengths (CL) of the corresponding peaks are calculated by the Scherrer's equation and summarized in Supplementary Table 1. The PEDOT:PSS film with 5% EG treatment exhibits the largest CL value compared to other films while the film with 90 °C annealing treatment also shows enhanced CL value. The enhanced π-π stacking in PEDOT is beneficial to the charge transport in the film, corresponding to the transconductance of p-OECTs.

Devices of g-OECT and c-OECT were fabricated to evaluate the electroanalytical performance by measuring the change of drain current when increasing the concentration of biomarkers. According to literature, the concentration of glucose and Ca^{2+} in tears are in the range of 0.1–0.6 mM and 0.4–1.1 mM, respectively[31,33]. The electrolyte concentration determines the Nernst potential, which affects the effective gate voltage and the consequent drain-source current. In addition, the response current shows a semilog-linear relationship towards the electrolyte concentration. The drain current response to the concentration is exhibited in Supplementary Fig. 4. Both devices show dropped drain current as the concentration increases while the g-OECT responds slowly due to the complex glucose redox reaction. We set the drain current measured at 0.1 mM condition as the reference point. As shown in Fig. 1e, the normalized current response (NCR) increases linearly with the exponential increase of the glucose and Ca^{2+} concentration. The fitted lines suggested the semilog-linear relationship, corresponding to the reported literatures. Compared to the g-OECT, the lower normalized current response of c-OECT may be attributed to the double electrical layers formed in the interface between the gold electrode and electrolyte[44–47], which leads to the decrease of effective gate voltage. Considering the interference of other positive ions in tears, such as potassium and sodium, the selectivity and specificity of the c-OECT is also evaluated. As shown in Fig. 1f and Supplementary Fig. 5, the addition of interfering ions exerts almost no effect on the drain current. Furthermore, the cross detection of glucose and Ca^{2+} is also assessed in the mixed artificial liquids. As shown in Supplementary Fig. 6, only several dozens of microamperes current variation can be observed. Considering the milliampere-level current changes at different concentrations, the addition of Ca^{2+} does not affect the glucose detection, nor does glucose for the Ca^{2+} detection.

Output characteristics matching between OECT sensors and OSCs

To maximize the response upon specific biomarkers, the sensors should be worked under the optimal operation voltages. For PEDOT:PSS-based OECTs at optimal working conditions, gate voltage is usually positive whereas the drain is negative. Therefore, we adopted OSCs with the inverted structure and normal structure to power the gate and drain, respectively. By sequential blade coating as shown in Fig. 2a, we achieved OSCs with different structures on the same substrate.

We further investigated the doping mechanism to confirm the suitable gate voltage. Time resolved UV-vis absorption spectra of the channel layer are carried out (Fig. 2b and Supplementary Fig. 7). The thin film displays a dominant absorption peak centered around 1000 nm at zero voltage bias, indicating the highly doped $PEDOT^+$ polaron state. The absorption peaks beyond 1000 nm indicates the presence of higher doped bipolaron state ($PEDOT^{2+}$)[48]. For glucose sensing OECT, the gate voltage must be larger than 0.6 V due to the redox reaction threshold. At 0.6 V

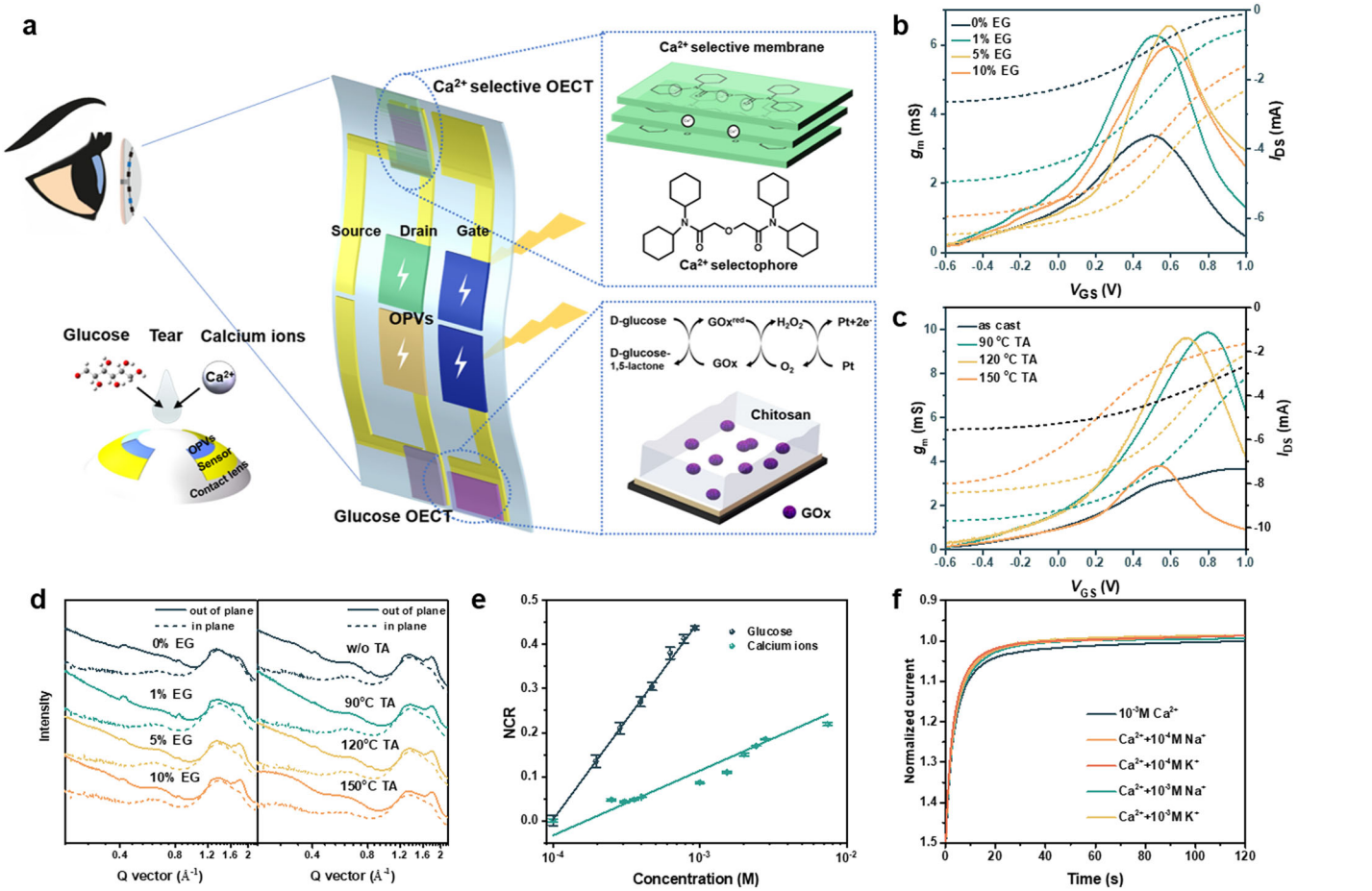

Fig. 1 Morphology optimization and electrical characterization. a Schematic of the integrated device and contact lens. The insets show the modification of electrode for Ca^{2+} and glucose sensor. **b** Transfer curves and related transconductance of the OECTs processed with different ethylene glycol ratio. **c** Transfer curves and related transconductance of the OECTs processed with different annealing temperature. The channel size of OECTs is 3 × 0.1 mm, measurements were carried out with 0.1 mM $CaCl_2$ aqueous solution under −0.2 V drain bias. **d** One dimensional GIWAXS line profiles of the corresponding processing conditions. **e** The normalized drain current response as a function of the concentration of glucose and Ca^{2+}. **f** The response of the calcium-selective OECT against sodium and potassium ions.

gate voltage, the bipolaronic states disappears with the emergence of a dominant absorption peak centered at 650 nm, corresponding to the neutral PEDOT° state, indicating $PEDOT^+$ and $PEDOT^{2+}$ states are effectively de-doped, leading to large g_m and thus high sensitivity.

For powering the gate electrode, since the gate current in OECTs is only several microamperes, much smaller than the short-circuit current of OSCs (100–200 μA), OSCs powering for gate electrode should work under nearly open-circuit circumstance. Therefore, OSCs with approximate 0.6 V open-circuit voltage (V_{OC}) under indoor illumination matches the gate power supply requirement. Here we select the PTB7-Th:ITIC[49] system with an inverted structure (ITO or PEDOT:PSS PH1000/ ZnO nanocrystals/ PTB7-Th:ITIC/MoO_x/ Al) as the gate power source. The *J-V* curves of PTB7-Th:ITIC system under simulator and LED illumination are shown in Fig. 2c and Supplementary Fig. 8. The open-circuit voltages dependent on the illumination power density are summarized in Fig. 2d. The open-circuit voltages are approaching to 0.6 V when the light density deceases to the indoor illumination density (500–2000 lux, the spectrum of the LED lamp is shown in Supplementary Fig. 9).

For powering the drain electrode, we first took the output characteristics of OSCs and p-OECTs into consideration. As shown in Fig. 2e, the operation voltage is decided by both the current of OECTs and OSCs. Since the gate voltage is set to be 0.6 V, or even larger, if the intersection is located at close to the V_{OC} point, the potential between gate and drain electrode will be larger than 1 V, which would cause water electrolysis and is detrimental to glucose test and may also cause eye decease. Although the V_{OC} of OSCs could be modulated to be less than 0.4 V using the interfacial layer with mismatched work-function, the 'S' shape *I-V* output characteristic may result in nonlinear current response to various concentrations. Under this consideration, the operation voltage should be modulated at the low voltage region. In this case, a rapid decrease of OSC current may contribute to the high current response in OECT sensors, contrary to the intuition that OSCs with good fill factor is more advantageous. As shown in Fig. 2e and Supplementary Table 2, larger current variation can be observed in P3HT:PCBM[50] system compared to the highly-efficient PM6:BTP4Cl-C24 system. Sensors powered by these two OSC systems are fabricated to further verify this inference. The current responses to different Ca^{2+} concentrations are exhibited in Supplementary Fig. 10 and the normalized current responses are displayed in Fig. 2f. As expected, a higher normalized current response values for sensor powered by P3HT:PCBM can be observed. The slope near the short-circuit current point in the *J-V* curve is related to the geminate recombination of OSC, which can be regulated by the film thickness. As shown in Fig. 2g, the current response can be enhanced by increasing the film thickness to 200 nm. However, further increase of film thickness cannot keep improving the current response. The relative current change for

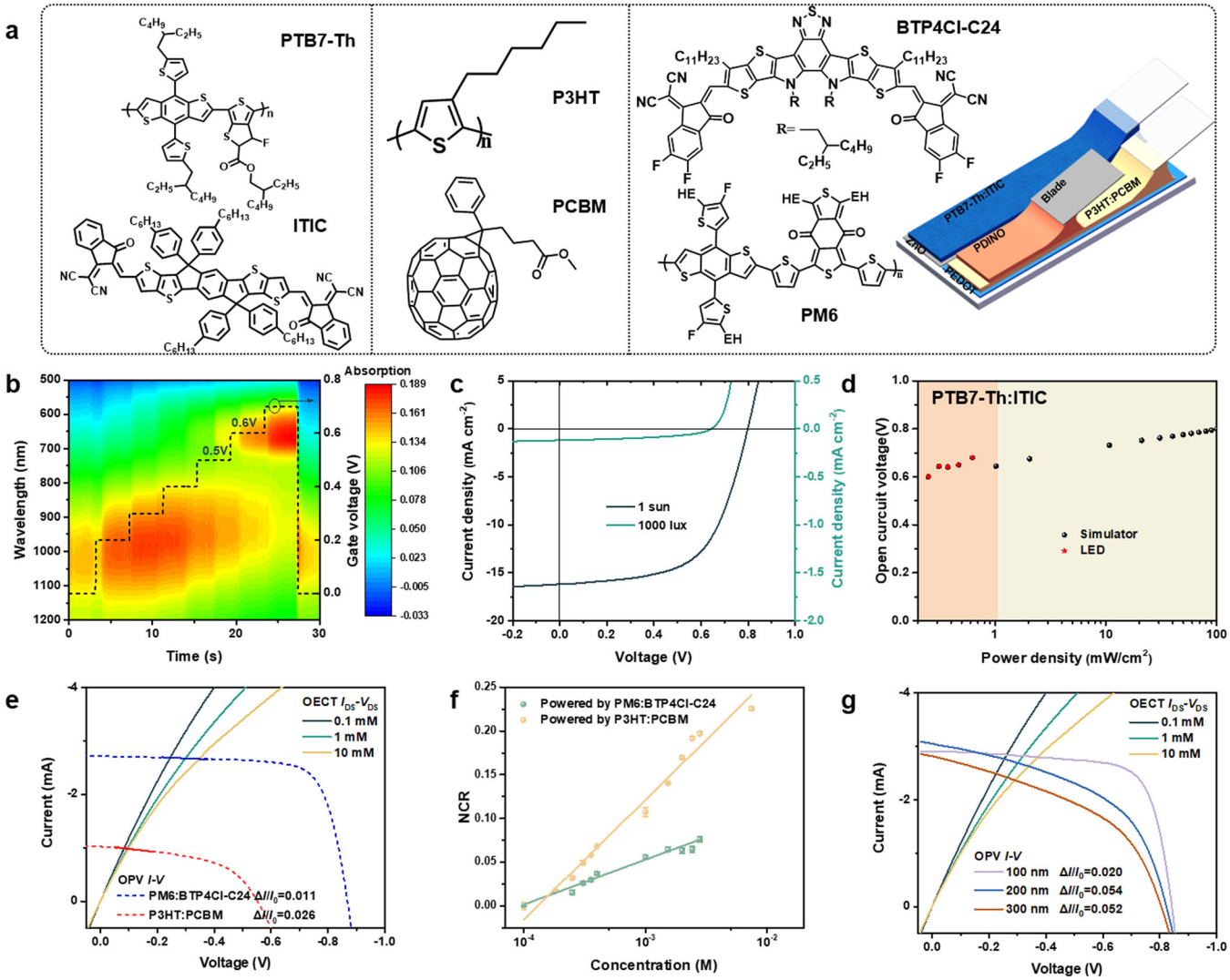

Fig. 2 Power output matching between OECT sensors and OSCs. a Chemical structures of the materials used for photovoltaic powering and the schematic of layer-by-layer blade coating. **b** Time resolved UV-vis absorption contour of the PEDOT:PSS channel with applied bias. **c** *J-V* curves of the gate OSCs under simulator and 1000 lux illumination. **d** The open circuit voltage of PTB7-Th: ITIC OSCs for gate powering under different light densities. The orange part is measured under LED illumination while the yellow part is measured under solar simulator illumination. **e** The output curves of p-OECT under 0.6 V gate voltage and the *I-V* curves of various OSCs under 1 sun light illumination. The I_0 is the intersection of the output curve of 0.1 mM and the current-voltage curve of OSC while ΔI is calculated by the intersections of 0.1 mM and 10 mM output curves. **f** The normalized current response to the Ca^{2+} concentration of p-OECTs powered by different drain OSCs. **g** The output characteristic curves of OECTs with different Ca^{2+} concentrations and current-voltage curves of OSCs with different film thickness.

300 nm device (0.052) decreases slightly compared to that of 200 nm device (0.054).

Testing of the self-powered integrated devices

The sensors and OSCs are then integrated into one self-powered electronics for further evaluation. Figure 3a shows the photo of the real device and the circuit model of the integrated device. The bottom electrodes of the OSCs are connected to the source electrodes of OECT sensors while the top electrodes are connected to gate and drain electrodes, respectively. Different from the reported self-powered OSCs/OECT devices[48,51,52], here both the gate and drain electrode are self-powered. As shown in Supplementary Fig. 11, the gate current of the self-powered system is merely about 20 nA, which is much smaller than the photocurrent at all illumination conditions, ensuring that the gate OSC works under the circumstance close to the open-circuit. Due to the weak current of OSC under indoor illumination, the measured drain current is only about several dozens of micro-amps, which is the same order of magnitude as the reported OECT devices powered by solar cells[48]. The inset in Fig. 3b shows the stability of gate voltage, which keeps almost as a constant with trifling spike mutations derived from the environmental shock possibly. The drain current of the PEDOT-OECT remains 98.5% of the initial values after continuous measurement for 30 min in air without any encapsulation, indicating decent stability of the integrated devices. The devices also show good stability over a span of time. After being tested daily for 7 days, the drain current remains over 92% of the initial values (shown in Supplementary Fig. 12). Furthermore, the test stability is evaluated by switching the LED lamp on and off repeatedly to simulate eyes opening and closing. The spectra of the LED light for integrated device illumination is shown in Supplementary Fig. 13. Since three different output light density can be tuned by the lamp, we can observe three response current as the light density changes. As shown in Supplementary Fig. 14, the measured drain current

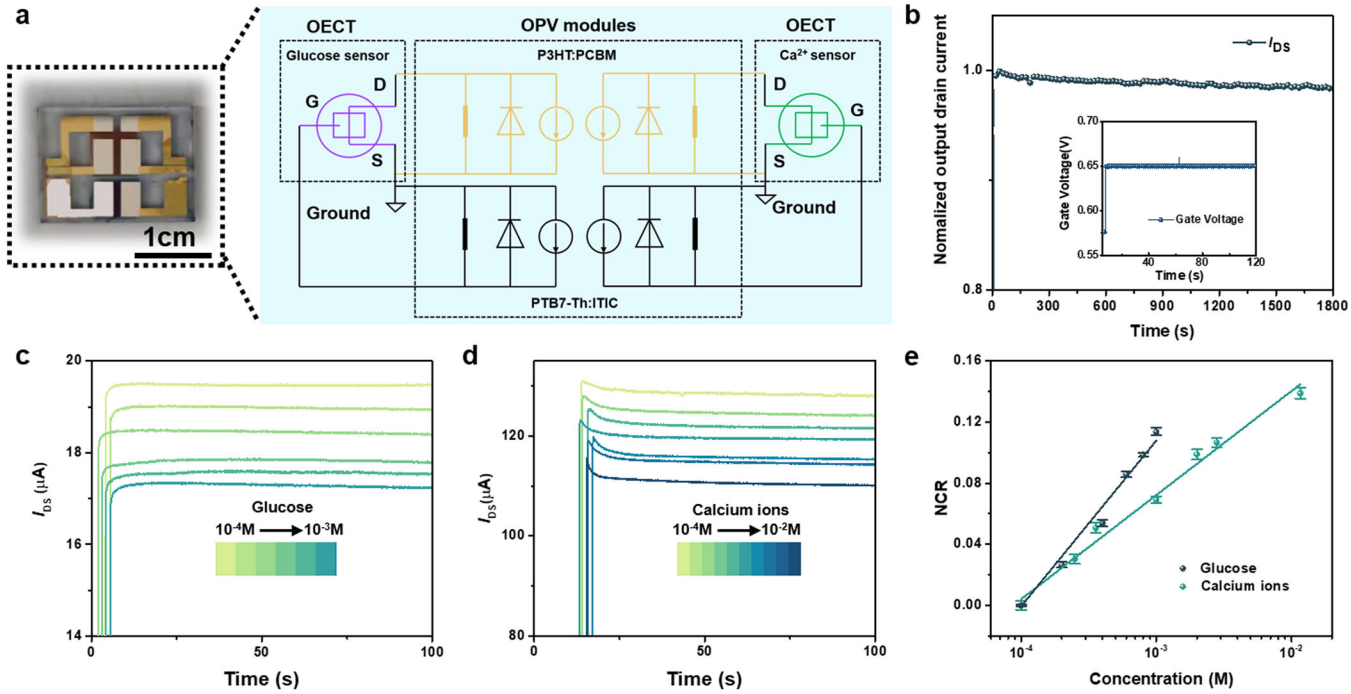

Fig. 3 Testing of the self-powered integrated devices. a The image of the self-powered integrated device and the equivalent circuit diagram of the integrated device. **b** The stability of the normalized output drain-current powered by OSC. The inset shows the stability of the gate voltage powered by OSCs. **c** The concentration-dependent drain current response of the glucose OECT powered by OSCs. **d** The concentration-dependent drain current response of the Ca^{2+} OECT powered by OSCs. **e** The normalized drain current response of the self-powered integrated device as a function of the concentration of glucose and Ca^{2+}.

under certain light density changes slightly, indicating good test stability of our integrated device. The effect of different light density on the normalized current response was also explored as shown in Supplementary Fig. 15. The drain current increases as the light density raises and semilog-linear relationship between normalized current response and concentration can be observed under different illumination densities. However, the response values under light intensity are slightly larger than those under high light intensities, probably due to the declined output of PCBM based OSCs when exposing to strong light for long time.

The electrical performance of the self-powered OECT sensors is further assessed. As shown in Fig. 3c, the drain current of the g-OECT drops from 19.5 to 17.2 μA as the glucose concentration increases from 0.1 mM to 1 mM. Similarly, the drain current drops from 127.9 to 110.2 μA as Ca^{2+} concentration increases from 0.1 mM to 10 mM (Fig. 3d). The potential measured between the gate and source also changes slightly as shown in Supplementary Fig. 16. The measured gate voltages are closed to the open-circuit voltage of gate OSCs, confirming our previous deduction that gate OSCs work under nearly open-circuit circumstance. We set the respective drain current measured at 0.1 mM as the reference value again and calibrate the normalized current response. As exhibited in Fig. 3e, both the self-powered sensors show a semilog-linear response to the concentration variations. About 13% average current variation can be observed when the glucose concentration changed by an order of magnitude. Similarly, about 15% average response drain current variation can be observed as Ca^{2+} concentration increased by two orders of magnitude. The response sensitivity of our device is comparable to those reported OECT sensors powered by source meter and biofuel cells[11,18]. Although the sensitivity and accuracy are inferior to AC coil powered sensors based on the mutual inductance principle, our self-powered device is more portable[26]. These results manifest that our self-powered sensors can be potential wearable electronics candidate for the long-term biomarker monitoring.

Remote monitoring and flexible integrated device

There have been lots of researches on the wireless communication between the sensors and portable devices through Bluetooth and the near filed communication (NFC) technique. Here we demonstrated that the sensing signals of our self-powered multiplexed device can be wireless communicated to the laptop as shown in Fig. 4a and Supplementary Fig. 17. A Si-based logic die (RF430FRK152H, Texas Instruments, USA) NFC chip together with a commercial developing board (MSP-EXP430G2) are linked with the self-powered OECT devices and resistors to digitize the measured data and transmit the information to the laptop. Since the NFC chip can only recognize the voltage signal. Resistors are linked with the drain and source electrode in series to convert the current signals into potential signals. The resistance values are evaluated by the potential between drain and source electrode and the drain current of respective OECT devices. Here the resistors used for g-OECT and c-OECT sensor are 20 kΩ and 3 kΩ, respectively. The radio frequency (RF) identification responses on laptop to the biomarkers with various concentration are exhibited in Supplementary Figs. 18–20. Due to the different potential difference between drain and source electrode for the g-OECT and c-OECT, a larger RF response value can be observed for c-OECT compared to the g-OECT. The RF responses to the concentration change are summarized in Fig. 4b and the semilog-linearly relationship can be surveyed for both the glucose and Ca^{2+} sensors. This result indicates the self-powered multiplexed sensing devices have great application potential in the next-generation wearable bioelectronics for long-term wireless monitoring.

To evaluate the application prospects of our multiplex sensors in ocular monitoring, tears were collected to measure the levels of glucose and Ca^{2+} in human bodies. We collected the tears from one laboratory member under fasting state when waking up and 1.5 h after breakfast since the glucose variation of tears should be behind than that of bloods. As shown in Fig. 4c and Supplementary Fig. 21, the concentration of glucose in tears is about

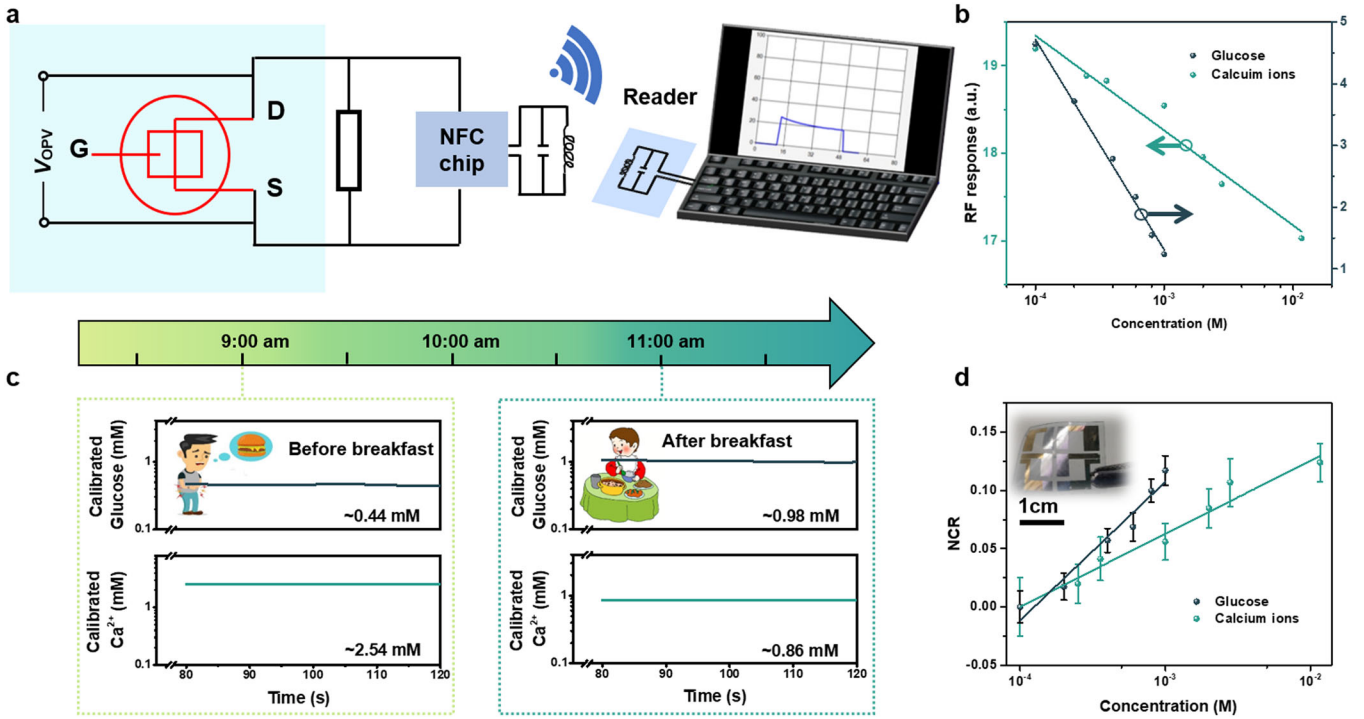

Fig. 4 Remote monitoring and flexible integrated device. a Circuit diagram connected with NFC chip and self-powered OECT sensor. **b** RFID response to the glucose and Ca^{2+} sensor under different concentrations. **c** The calibrated concentration of glucose and Ca^{2+} in human tears. The tears are collected before breakfast and 1.5 h after breakfast separately. **d** The normalized current response of the flexible integrated device.

0.74 ± 0.03 mM and it raises up to about 0.97 ± 0.05 mM after having breakfast. It has been reported that the glucose concentration in tears is about 0.1–0.3 mM for normal people and about 1 mM for diabetics under fasting state[53–55]. The concentration variation after meals should be less than 67% for normal people. The detection concentrations by our device are on the same order of magnitude as the literature reported (0.1–0.6 mM). The slightly higher detection concentration may be attributed to the tears collection method according to the literatures. The contents of Ca^{2+} are also tested from the same tears and the calibrated results indicate that the Ca^{2+} concentrations are about 1.15 ± 0.01 mM and 0.98 ± 0.01 mM before and after meals, respectively, which is on the same order of magnitude as the literature reported (0.4–1.1 mM)[56–58]. For normal people, the concentration of Ca^{2+} in tears decreases mildly at noon compared to that in the morning. The detection errors possibly come from the response current fluctuation and the calibration error. The collection process and the small sampling size also limit the detection accuracy since we did not measure in eyes directly. In addition, the light density used for measurement as shown in Supplementary Fig. 13 and device variation also contributes to the detection errors. Nevertheless, these results have demonstrated the potential application of the self-powered sensors in future ophthalmic diagnosis.

After the demonstration of self-powered multiplex sensors on the glass substrate, we further fabricated the flexible self-powered devices. We used PH1000 on 200 μm polydimethylsiloxane (PDMS) substrate to replace the ITO/glass substrate. A photograph of the flexible device is shown as the inset in the Fig. 4d. The sensing signals towards different biomarkers concentration are shown in Supplementary Fig. 22. Compared to the rigid devices, the drain current response curves are more unstable and smaller. Based on the results, similar normalized current responses are calculated as shown in Fig. 4d. Due to the unstable current response, large error bars can be observed which is disadvantageous to the detection. One of the reasons for the high noise in the flexible sensors is the weak power supply from the flexible OSCs. In addition, the deformation of the flexible sensors might also contribute to the poor signal quality since the loose contact of the sensors will result in electrical noises. To make the sensors work better, more flexible circuit elements such as rectifying circuits should be integrated into the overall biosensor systems in future works.

In conclusion, we demonstrated a flexible self-powered multiplexed OECT sensing device for monitoring the concentration of glucose and Ca^{2+} in tear fluids. The integrated device was fabricated via simple process including solution blade-coating and thermal evaporation, indicating great potential for batch production. The morphology of the OECT channel layer and operation voltage of the sensors are investigated to obtain sensitive responses to the concentration variation of biomarkers under large range of illumination conditions from sun light to indoor light. To meet the powering requirements of OECT sensors, the output of the OSCs is optimized by the matching of photovoltaic active layers and selection of transport interfacial layers without using other circuit elements such as resistors and capacitors. The integrated device can work under the illumination indoor lights, exhibiting good responses to the concentration change of glucose and Ca^{2+}. The synergetic measurements of multiple biomarkers will help to the monitoring and diagnosis of diabetes. The sensing information can be transmitted to the portable devices wirelessly by the integrated NFC unit. This self-powered multiplexed sensing device is prospective to be equipped on the contact lens and pave the wave of next-generation wearing bioelectronics for the long-term noninvasive in vivo surveillance and diagnosis.

METHODS

Materials

PTB7-Th, ITIC, P3HT, PCBM, PM6, and PDINO are purchased from Solarmer Materials Inc. Chlorobenzene (CB), 1-Chloronaphthalene (1-CN), ethylene

glycol (EG) (3-glycidyloxypropyl) trimethoxysilane (GOPS), dodecylbenzene sulfonic acid (DBSA), tetrahydrofuran (THF), calcium ionophore II (ETH 129), bis(2-ethylhexyl) adipate, potassium tetrakis (4-chloropheny1) borate (KT4ClPB), glucose oxidases (GOx), chitosan, isopropanol, dimethyl sulfoxide (DMSO) and acetic acid are purchased from Sigma-Aldrich and Aladdin. PEDOT:PSS AL4083 and PEDOT:PSS PH1000 are purchased from Clevios. BTP4Cl-C24 is synthesized by Kai Chen by changing the side chain of BTP4Cl according to the literature. All chemicals used as received without further purification.

Fabrication of the OSCs

The patterned ITO glass substrate was sequential cleaned by sonication in detergent water, deionized water, acetone and isopropanol for 20 min of each steps. After UVO treatment for 20 min, ZnO precursor was bladed-coated on the cleaned ITO substrate to form a 20 nm thickness and 5 mm width electron-transporting layer, followed by thermal annealing at 200 °C for 30 min. The coating speed was 7 mm s^{-1} on the 50 °C substrate with 100 μm gap. Then PEDOT:PSS AL4083 was coated also to form a 20 nm thickness and 5 mm width hole-transporting layer, followed by thermal annealing at 140 °C for 10 min. The coating speed was 8 mm s^{-1} on the 60 °C substrate with 100 μm gap. For the active layer solution, PTB7-Th:ITIC was prepared at a total concentration of 23 mg mL^{-1} (donor: acceptor = 1:1.3 by weight) in CB solvent while P3HT:PCBM was prepared at a total concentration of 30 mg mL^{-1} (donor: acceptor = 1:1 by weight) in CB solvent with 1.2 vol% 1-CN. PM6:BTP4Cl-C24 was prepared at a total concentration of 20 mg mL^{-1} (donor: acceptor = 1:1 by weight) in CB solvent. Films are blade-coated on the 60 °C substrate to form a 100 nm photovoltaic layer. Then the films are vacuum treated for 1 h to remove the 1-CN additive. After thermal annealing at 100 °C for 10 min, the PDINO layers was blade-coated on the room temperature substrate with 6 mm s^{-1} speed and 50 μm gap. Finally, a 10 nm MoO_3 and 100 nm Al were sequentially thermal deposited with masks below the vacuum level of 1×10^{-4} Pa.

Fabrication of the OECT sensors

The OECT sensors were fabricated on the OSC device subsequently. A 10 nm of Cr layer as adhesion promoter and 80 nm Au layer were thermal deposited. For the glucose sensor, the Au gate was replaced by 100 nm Pt layer by magnetron sputtering on the Cr layer. PEDOT:PSS PH1000 was mixed with EG (0 vol%, 1 vol%, 5 vol%, 10 vol%), GOPS (1 vol%) and DBSA (0.1 vol%). After that, the mixed PH1000 solution was coated as the active channel and follower by thermal annealing for 30 min. For the calcium ions sensors, the ionically selective membranes were coated on the top of PH1000 channel with the mixture of THF (2 mL) containing a high-molecular weight PVC (63 mg), calcium ionophore II (ETH129, 4 mg), the bis (2-ethylhexyl) plasticizing solvent mediator (120 μL) and the anion excluder potassium tetrakis (4-chloropheny1) borate (4 mg). For glucose sensors, GOx solution was prepared by dissolving 30 mg of GOx in 2 mL of a PBS solution. A chitosan solution was prepared by dissolving chitosan in an acetic acid solution (0.05 M) followed by electromagnetic stirring for 1 h. After that, The GOx solution was mixed with the chitosan solution with the ratio of 1:1 followed by sonication for 30 min before use. The GOx-chitosan mixture solution was drop casted onto the PT gate and dried in glove box overnight. The device was rinsed in DI water to remove any non-immobilized enzymes before testing.

Fabrication of the flexible devices

The purchased PDMS membranes with 200 μm were first immersed in CB solvent for 5 min followed by washing in isopropanol for 30 s. Then the membranes were pasted on the glass substrates to finish the coating steps. PDMS membranes were plasma treated for 6 min. After that, the mixed PH1000 solution containing 5% DMSO and 2% Dupont Zonyl FS300 was coated to make the electrode on PDMS substrate. The mixed solution was spin-coated at 3000 rpm twice and followed by thermal annealing at 140 °C for 20 min. Then the films were dipped in acetic acid for 6 min and annealed on 80 °C hotplate for 15 min to remove residual acid to enhance the conductivity. For OSCs fabrication, ZnO nanocrystals were used as the interfacial layer to avoid annealing under high temperature. The remaining process was the same as that of the rigid devices.

Device characterizations

The *J–V* characteristics of OSCs were performed in N_2-filled glovebox under AM 1.5 G (100 mW cm^{-2}) using a AAA solar simulator (SS-F5-3A, Enli Technology CO., Ltd.) calibrated by a standard Si photovoltaic cell with a KG5 filter. The measurements were recorded by a Keithley 2400 source meter unit. For indoor lighting measurements, an indoor LED lamp with a 4000 K color temperature was used.

The *I-V* characteristics of OECTs were measured with a Keithley 2602B 22 Source/Measurement Unit (SMU) using two channels. One channel powered the drain electrode and measured the source-drain current while the other channel powered the gate electrode. For the OSC-powered devices, only one channel was used as an ampere meter to measure the I_{DS}. All tests were done with analytes in PBS electrolytes or deionized water electrolytes excepted the tear fluids, which were collected from humans under the stimulus by lachrymator.

The response of the device to different calcium ions and glucose concentrations was normalized. The average response results and standard deviations were calculated from the last 20 s data of each measurements and the response at 0.1 mM was set as I_0. The normalized current response (NCR) was determined by the following equation:

$$NCR = \left| \frac{I - I_0}{I_0} \right| \quad (1)$$

The RFID measurements was carried out by the open software RF430FRL 15xH Default Projects (Texas Instruments). The software was not further developed by our lab. The reading value was dependent on the voltage on the series resistor and each unit value on the RF reader was corresponding to about 0.011 V voltage on the series resistance. The resistor was connected to the channel by wires.

DATA AVAILABILITY

The experimental data that support the findings of this study are available from the corresponding author upon reasonable request.

Received: 30 March 2022; Accepted: 5 August 2022;
Published online: 25 August 2022

REFERENCES

1. Jang, J. et al. Human-interactive, active-matrix displays for visualization of tactile pressures. *Adv. Mater. Technol.* **4**, 1900082 (2019).
2. Yoo, Y. J. et al. Large-area virus coated ultrathin colorimetric sensors with a highly lossy resonant promoter for enhanced chromaticity. *Adv. Sci.* **7**, 2000978 (2020).
3. Gao, W. et al. Fully integrated wearable sensor arrays for multiplexed in situ perspiration analysis. *Nature* **529**, 509–514 (2016).
4. Ershad, F. et al. Ultra-conformal drawn-on-skin electronics for multifunctional motion artifact-free sensing and point-of-care treatment. *Nat. Commun.* **11**, 1–13 (2020).
5. Kim, D.-H. et al. Epidermal electronics. *Science* **333**, 838–843 (2011).
6. Nair, V. et al. Laser writing of nitrogen-doped silicon carbide for biological modulation. *Sci. Adv.* **6**, eaaz2743 (2020).
7. Sim, K. et al. Fully rubbery integrated electronics from high effective mobility intrinsically stretchable semiconductors. *Sci. Adv.* **5**, eaav5749 (2019).
8. Xiong, J., Thangavel, G., Wang, J., Zhou, X. & Lee, P. S. Self-healable sticky porous elastomer for gas-solid interacted power generation. *Sci. Adv.* **6**, eabb4246 (2020).
9. Koo, J. H. et al. Wearable electrocardiogram monitor using carbon nanotube electronics and color-tunable organic light-emitting diodes. *Acs Nano* **11**, 10032–10041 (2017).
10. Lee, H. et al. Toward all-day wearable health monitoring: An ultralow-power, reflective organic pulse oximetry sensing patch. *Sci. Adv.* **4**, eaas9530 (2018).
11. Lee, H. et al. A graphene-based electrochemical device with thermoresponsive microneedles for diabetes monitoring and therapy. *Nat. Nanotech.* **11**, 566–572 (2016).
12. Yetisen, A. K. et al. Reusable, robust, and accurate laser-generated photonic nanosensor. *Nano Lett.* **14**, 3587–3593 (2014).
13. Wustoni, S., Savva, A., Sun, R., Bihar, E. & Inal, S. Enzyme-free detection of glucose with a hybrid conductive gel electrode. *Adv. Mater. Interfaces* **6**, 1800928 (2018).
14. Kim, J. et al. Wearable smart sensor systems integrated on soft contact lenses for wireless ocular diagnostics. *Nat. Commun.* **8**, 1–8 (2017).
15. Kondo, M. et al. Imperceptible magnetic sensor matrix system integrated with organic driver and amplifier circuits. *Sci. Adv.* **6**, eaay6094 (2020).
16. Wang, S. et al. Skin electronics from scalable fabrication of an intrinsically stretchable transistor array. *Nature* **555**, 83–88 (2018).

17. Falk, M. et al. Biofuel cell as a power source for electronic contact lenses. *Biosens. Bioelectron.* **37**, 38–45 (2012).
18. You, Y. U. et al. Biofuel-powered soft electronic skin with multiplexed and wireless sensing for human-machine interfaces. *Sci. Robot.* **5**, eaaz7946 (2020).
19. Ohayon, D. et al. Biofuel powered glucose detection in bodily fluids with an n-type conjugated polymer. *Nat. Mater.* **19**, 456–463 (2020).
20. Reid, R. C., Minteer, S. D. & Gale, B. K. Contact lens biofuel cell tested in a synthetic tear solution. *Biosens. Bioelectron.* **68**, 142–148 (2015).
21. Nasreldin, M. et al. Flexible micro-battery for powering smart contact lens. *Sensors* **19**, 2062 (2019).
22. Kim, C. Y. et al. Soft subdermal implant capable of wireless battery charging and programmable controls for applications in optogenetics. *Nat. Commun.* **12**, 1–13 (2021).
23. Minjae, K. U. et al. Smart, soft contact lens for wireless immunosensing of cortisol. *Sci. Adv.* **6**, eabb2891 (2020).
24. Keum, D. H. et al. Wireless smart contact lens for diabetic diagnosis and therapy. *Sci. Adv.* **6**, eaba3252 (2020).
25. Won, S. M., Cai, L., Gutruf, P. & Rogers, J. A. Wireless and battery-free technologies for neuroengineering. *Nat. Biomed. Eng.* 1–19 (2021).
26. Park, J. et al. Soft, smart contact lenses with integrations of wireless circuits, glucose sensors, and displays. *Sci. Adv.* **4**, eaap9841 (2020).
27. Jang, J. et al. Smart contact lens and transparent heat patch for remote monitoring and therapy of chronic ocular surface inflammation using mobiles. *Sci. Adv.* **7**, eabf7194 (2021).
28. Park, J. et al. Printing of wirelessly rechargeable solid-state supercapacitors for soft, smart contact lenses with continuous operations. *Sci. Adv.* **5**, eaay07641 (2019).
29. Jung, H. J., Abou-Jaoude, M., Carbia, B. E., Plummer, C. & Chauhan, A. Glaucoma therapy by extended release of timolol from nanoparticle loaded silicone-hydrogel contact lenses. *J. Control. Release* **165**, 82–89 (2013).
30. Yuan, M. et al. Electronic contact lens: a platform for wireless health monitoring applications. *Adv. Intell. Syst.* **2**, 1900190 (2020).
31. Kim, J., Cha, E. & Park, J. U. Recent advances in smart contact lenses. *Adv. Mater. Technol.* **5**, 201900728 (2019).
32. Ma, X. et al. Smart contact lenses for biosensing applications. *Adv. Intell. Syst.* **3**, 202000263 (2021).
33. Farandos, N. M., Yetisen, A. K., Monteiro, M. J., Lowe, C. R. & Yun, S. H. Contact lens sensors in ocular diagnostics. *Adv. Healthc. Mater.* **4**, 792–810 (2015).
34. Becerra-Tomás, N. et al. Increased serum calcium levels and risk of type 2 diabetes in individuals at high cardiovascular risk. *Diabetes Care* **37**, 3084–3091 (2014).
35. Pittas, A. G., Lau, J., Hu, F. B. & Dawson-Hughes, B. The role of vitamin D and calcium in type 2 diabetes. A systematic review and meta-analysis. *J. Clin. Endocrinol. Metab.* **92**, 2017–2029 (2007).
36. Keene, S. T. et al. Wearable organic electrochemical transistor patch for multiplexed sensing of calcium and ammonium ions from human perspiration. *Adv. Healthc. Mater.* **8**, e1901321 (2019).
37. Pierre, A., Doris, S. E., Lujan, R. & Street, R. A. Monolithic integration of ion-selective organic electrochemical transistors with thin film transistors on flexible substrates. *Adv. Mater. Technol.* **4**, 1800577 (2019).
38. Li, Y. et al. Ion-selective organic electrochemical transistors: recent progress and challenges. *Small* **18**, 2107413 (2022).
39. Liu, Y. et al. Self-powered artificial joint wear debris sensor based on triboelectric nanogenerator. *Nano Energy* **85**, 105967 (2021).
40. Petritz, A. et al. Imperceptible energy harvesting device and biomedical sensor based on ultraflexible ferroelectric transducers and organic diodes. *Nat. Commun.* **12**, 2399 (2021).
41. Kim, S.-M. et al. Influence of PEDOT: PSS crystallinity and composition on electrochemical transistor performance and long-term stability. *Nat. Commun.* **9**, 1–9 (2018).
42. Liu, F., Gu, Y., Jung, J. W., Jo, W. H. & Russell, T. P. On the morphology of polymer-based photovoltaics. *J. Polym. Sci., Part B: Polym. Phys.* **50**, 1018–1044 (2012).
43. Hexemer, A. et al. A SAXS/WAXS/GISAXS beamline with multilayer monochromator. *J. Phys.: Conf. Ser.* **247**, 012007 (2010).
44. Lin, P., Yan, F. & Chan, H. L. Ion-sensitive properties of organic electrochemical transistors. *ACS Appl. Mater. Interfaces* **2**, 1637–1641 (2010).
45. Cicoira, F. et al. Influence of device geometry on sensor characteristics of planar organic electrochemical transistors. *Adv. Mater.* **22**, 1012–1016 (2010).
46. Tarabella, G. et al. Effect of the gate electrode on the response of organic electrochemical transistors. *Appl. Phys. Lett.* **97**, 205 (2010).
47. Bernards, D. A. et al. Enzymatic sensing with organic electrochemical transistors. *J. Mater. Chem.* **18**, 116–120 (2008).
48. Surendran, A. et al. Self-powered organic electrochemical transistors with stable, light-intensity independent operation enabled by carbon-based perovskite solar cells. *Adv. Mater. Techno.* **6**, 2100565 (2021).
49. Zhao, F. et al. Single-junction binary-blend nonfullerene polymer solar cells with 12.1% efficiency. *Adv. Mater.* **29**, 1700144 (2017).
50. Cardozo, O., Farooq, S., Stingl, A. & Fraidenraich, N. Investigation of performance of P3HT:PCBM organic photovoltaic module under real operating conditions. *Sol. Energy* **190**, 543–548 (2019).
51. Park, S. et al. Self-powered ultra-flexible electronics via nano-grating-patterned organic photovoltaics. *Nature* **561**, 516–521 (2018).
52. Choi, J. et al. Wearable self-powered pressure sensor by integration of piezo-transmittance microporous elastomer with organic solar cell. *Nano Energy* **74**, 104749 (2020).
53. Sen, D. & Sarin, G. Tear glucose levels in normal people and in diabetic patients. *Br. J. Ophthalmol.* **64**, 693–695 (1980).
54. Zhang, J., Hodge, W., Hutnick, C. & Wang, X. Noninvasive diagnostic devices for diabetes through measuring tear glucose. *J. diabetes Sci. Technol.* **5**, 166–172 (2011).
55. Van Haeringen, N. J. Clinical biochemistry of tears. *Surv. Ophthalmol.* **26**, 84–96 (1981).
56. Huth, S. W., Hirano, P. & Leopold, I. H. Calcium in tears and contact lens wear. *Arch. Ophthalmol.* **98**, 122–125 (1980).
57. Winder, A., Ruben, M. & Sheraidah, G. Tear calcium levels and contact lens wear. *Br. J. Ophthalmol.* **61**, 539–543 (1977).
58. Avisar, R., Savir, H., Sidi, Y. & Pinkhas, J. Tear calcium and magnesium levels of normal subjects and patients with hypocalcemia or hypercalcemia. *Investig. Ophthalmol. Vis. Sci.* **16**, 1150–1151 (1977).

ACKNOWLEDGEMENTS

Thanks for the support from National Natural Science Foundation of China (21704082, 21875182), Key Scientific and Technological Innovation Team Project of Shaanxi Province (2020TD-002), 111 project 2.0 (BP2018008). X-ray data was acquired at beamlines 7.3.3 at the Advanced Light Source, which is supported by the Director, Office of Science, Office of Basic Energy Sciences, of the U.S. Department of Energy under Contract No. DE-AC02-05CH11231. The authors thank Dr. Eric Schaible and Dr. Chenhui Zhu at beamline 7.3.3, for assistance with data acquisition.

AUTHOR CONTRIBUTIONS

B.L. and M.W. contribute equally to this work. W.M. and L.W. directed this work. B.L. and M.W. conducted experiments, fabricated devices, and analyzed data. C.Z. helped to analyze the data. S.W., X.L., and Z.L. helped the device fabrication. K.C. provided the materials. C.Z., X.S. and S.Y. built the wireless communication. All the authors co-wrote the manuscript.

COMPETING INTERESTS

The authors declare no competing interests.

ADDITIONAL INFORMATION

Supplementary information The online version contains supplementary material available at https://doi.org/10.1038/s41528-022-00211-6.

Correspondence and requests for materials should be addressed to Laili Wang or Wei Ma.